

# Effect of functionalization on the self-assembling propensity of $\beta$ -sheet forming peptides†

Francesca Taraballi,<sup>ab</sup> Marcello Campione,<sup>a</sup> Adele Sassella,<sup>a</sup> Angelo Vescovi,<sup>b</sup> Alberto Paleari,<sup>a</sup> Wonmuk Hwang<sup>c</sup> and Fabrizio Gelain<sup>\*b</sup>

Received 11th June 2008, Accepted 1st October 2008

First published as an Advance Article on the web 18th November 2008

DOI: 10.1039/b809236b

The mechanism underlying self-assembly of short peptides has not been fully understood despite the fact that a few decades have passed since their serendipitous discovery. RADA16-I (AcN-RADARADARADARADA-CONH<sub>2</sub>), representative of a class of self-assembling peptides with alternate hydrophobic and hydrophilic residues, self-assembles into  $\beta$ -sheet bilayer filaments. Though a sliding diffusion model for this class of peptides has been developed in previous works, this theory need further improvements, supported by experimental investigations, to explain how RADA16-I functionalization with biological active motifs, added at the C-terminus of the self-assembling core sequence, may influence the self-assembling tendency of new functionalized peptides (FPs). Since FPs recently became a promising class of biomaterials for cell biology and tissue engineering, a better understanding of the phenomenon is necessary to design new scaffolds for nanotechnology applications. In this work we investigated *via* atomic force microscopy and Raman spectroscopy the assembly of three RADA16-I FPs that have different hydrophobic/hydrophilic profiles and charge distributions. We performed molecular dynamics simulations to provide further insights into the experimental results: functionalizing self-assembling peptides can strongly influence or prevent molecular assembly into nanofibers. We also found certain vibrational molecular modes in Raman spectroscopy to be useful indicators for elucidating the assembly propensity of FPs. Preliminary FP designing strategies should therefore include functional motif sequences with balanced hydrophobicity profiles avoiding hydrophobic patches, causing fast hydrophobic collapses of the FP molecules, or very hydrophilic motifs capable of destabilizing the RADA16-I double layered  $\beta$ -sheet structure.

## Introduction

Synthetic polymers and biodegradable materials have had a significant impact in medicine over the past thirty years and the micro and nano-fabrication of new biomaterials stimulates growing interest among many scientific and medical communities.<sup>1</sup> In particular, molecular self-assembly is a promising approach for the fabrication of new nanostructured scaffolds with customizable mechanical properties and biological functions.<sup>2,3</sup> Self-assembly is mediated by various non covalent interactions such as electrostatic, hydrogen bonding, hydrophobic, hydrophilic, and van der Waals interactions.<sup>4</sup> Subtle balance among these interactions determines the assembly

propensity of the molecules and the resulting supramolecular structure. In this regard, self-assembling peptides have drawn attention for nearly two decades<sup>5</sup> as their sequence can be prescribed to generate materials with defined molecular properties. They have a wide range of applications, that include tissue regeneration,<sup>6</sup> drug delivery,<sup>7</sup> protein crystallization,<sup>8</sup> and cellular internalization.<sup>9</sup> Furthermore, these peptides are highly biocompatible, can be easily synthesized on a large scale and purified to meet clinical application standards in the near future.

An extensively characterized and recently commercialized class of self-assembling peptides includes RADA16-I (Fig. 1a), RADA16-II, EAK16, KLDL.<sup>10</sup> They are typically 12–30 residues in length and have self-complementary sequences (alternating hydrophobic and hydrophilic residues), which causes one side of the peptide to be hydrophobic, and the other side hydrophilic, so that, in physiological solutions, they spontaneously assemble into  $\beta$ -sheet bilayer nanofibers.<sup>11,12</sup> Networks of these filaments form hydrogels which are 99% made of water.<sup>13</sup> Self-assembled nanofibers show the cross- $\beta$  molecular structure of amyloid fibrils,<sup>14,15</sup> thus proving themselves as useful in vitro models for amyloid fibrillogenesis related diseases, such as Alzheimer's or Huntington's diseases.<sup>16</sup>

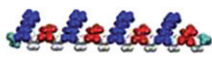
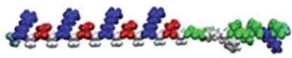
RADA16-I has been used as a three-dimensional cell culture scaffold for endothelial cells,<sup>17</sup> neural progenitor cells,<sup>18</sup> cardiac myocytes,<sup>19</sup> etc. The hydrogel can be customized for specific applications by linking various functional groups at the N- and

<sup>a</sup>Department of Materials Science, University of Milan - Bicocca, via R. Cozzi 53, 20125 Milan, Italy. E-mail: francesca.taraballi@mater.unimib.it; Fax: +0039 02 64485400; Tel: +0039 02 64485169

<sup>b</sup>Department of Biotechnology and Bioscience, University of Milan - Bicocca, piazza della Scienza 2, 20125 Milan, Italy. E-mail: fabrizio.gelain@unimib.it; Fax: +0039 02 64483321; Tel: +0039 02 64483312

<sup>c</sup>Department of Biomedical Engineering, Texas A&M University, Zachry Engineering Center 337, College Station, 77843-3120 Texas, U.S.A. E-mail: hwm@tamu.edu; Fax: +1-979-458-0178; Tel: +1-979-458-0178

† Electronic supplementary information (ESI) available: Hydrophobicity profiles using the Kyte-Doolittle scale; starting structure of each peptide before the MD simulations; tapping mode image of RADA16-I-ALK at 1% (w/v); and AFM image of monolayer formed by RADA16-I-SDE over mica surface. See DOI: 10.1039/b809236b

A	RADA16-I	Ac-RADARADARADARADA-COIH2	
	RADA16-I-BMHP1	Ac-RADARADARADARADA-GGPFSSSTKTCOIH2	
	RADA16-I-ALK	Ac-RADARADARADARADA-GGALKRQGRRTLYGF-COIH2	
	RADA16-I-SDE	Ac-RADARADARADARADA-GGSDSHHSDESDE-COIH2	

### Hydrophobicity profiles

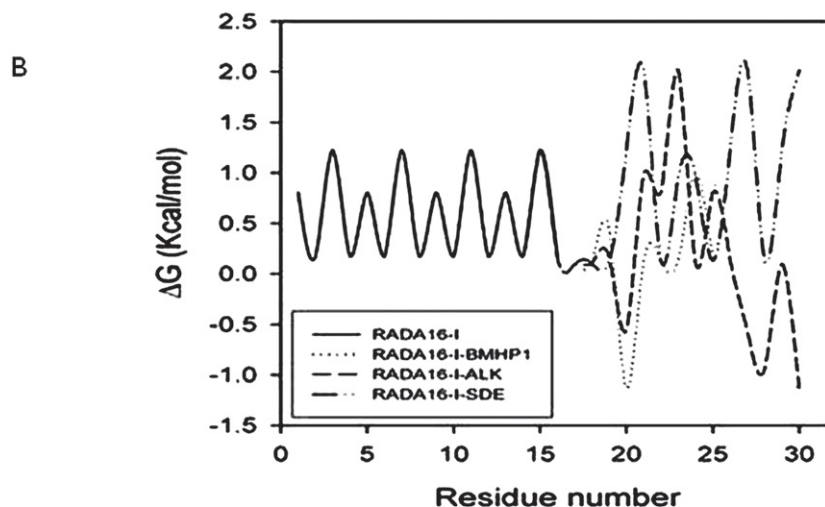


**Fig. 1** (A) The peptides used in this study. In the self-assembling “core” sequence basic residues (blue) alternate with acid residues (red) and hydrophobic ones (white). Polar neutral residues (green) are present in added functional motifs. A spacer of two glycines has been added between the self-assembling cores and the functional motifs. (B) Superimposed hydrophobicity profiles of the tested peptides (see methods for details), positive values testify hydrophilic residues while negative ones are for hydrophobic patches.

C-terminus.<sup>20</sup> Previously, we analyzed the bioactivity of functionalized RADA16-I by attaching 6- to 15-residues derived from various extracellular matrix molecules and growth factors.<sup>21,22</sup> RADA16-I has been chosen as a self-assembling core to which a spacer consisting of two glycines and various biologically active motifs can be attached.<sup>21</sup> The Gly-Gly spacer is adopted to provide the FP with a highly flexible linker connecting the RADA16-I sequence, that is the assembling portion of FP, and the functional motif. This flexibility is considered as fundamental for the correct exposure of the functional motif to cell membrane receptors.<sup>21</sup> When RADA16-I is functionalized with the bone marrow homing peptide BMHP1 (PFSSTKT), it is capable of stimulating neural stem cell adhesion, proliferation and differentiation; when extended with bone-cell secreted signal peptide ALK (ALKRQGRRTLYGF) it promotes mouse osteoblast proliferation and differentiation;<sup>22</sup> while the functionalization with the osteopontin derived peptide sequence SDE (SDESHHSDESDE), a bone ECM molecule regulating cell adhesion, migration and survival,<sup>22</sup> is a FP newly designed for bone regeneration applications.

Although our previous studies demonstrated the potential of FPs, they also suggested that different functional motifs

significantly influence the propensity for self-assembly and the overall mechanical properties of the scaffold at the meso-scale.<sup>21</sup>

To address this issue, we investigated the three above-mentioned RADA16-I derived FPs (see Fig. 1a) by using a combination of material characterization techniques and molecular dynamic simulations. Notwithstanding RADA16-I has been characterized in various studies, the other FPs, derived from the same 16-mer core, still have to be fully characterized and their self-assembly explained. The three FPs tested differ in length, charge distribution, and hydrophobicity. The stability of the cross- $\beta$  structure of each peptide was investigated using MD simulations. We also analyzed the assembled structures *via* Raman spectroscopy and atomic force microscopy (AFM), which were consistent with the “*in silico*” findings.

Raman micro-spectroscopy, a well-established technique already applied to characterize the molecular structure of proteins like amyloid protein  $\alpha$ -synuclein,<sup>23</sup> has been used to investigate in a greater detail the secondary structure of the self-assembling peptides. As the same experimental conditions were adopted in all tests, the Raman spectra and AFM nanostructure morphologies analyzed can be directly correlated. Our

results indicate that hydrophobicity of the functional group is a major factor responsible for the overall assembly: functionalization with too hydrophilic or too hydrophobic groups does not lead to filament assembly. Thus, when designing a FP, the sequence of the base peptide and the linker between the base peptide and the functional group must be adjusted to accommodate the hydrophobicity of the functional group, or *vice versa*. Lastly our work indicated Raman spectroscopy as a powerful technique for assessing peptide assembly in aqueous solutions, results confirmed and supported by MD and AFM tests. When applied to a wide spectrum of FPs, the synergistic use of computational and experimental modalities would be useful in elucidating their design principles.

## Experimental

### Materials synthesis

RADA16-I solution (1%), commercially available as PuraMatrix was purchased from BD Bioscience, Bedford, MA. The functionalized designer peptides were custom-synthesized with a CEM Liberty Microwave Peptide Synthesizer (Matthews, NC). Peptides were identified by a MALDI-TOF mass spectrometer. All FPs were purified by HPLC in CH<sub>3</sub>CN/water gradient and dissolved in water at a final concentration of 1% (w/v). The peptide solution was sonicated for 20 min prior usage.

### Hydrophobicity profiles

We used hydrophobicity scale proposed by White and Winmley:<sup>24</sup> hydrophilic (hydrophobic) residues have positive (negative) values (Fig. 1b) experimentally determined as transfer free energies. The Kyte–Doolittle scale was used as an additional confirmation of the obtained profiles (ESI, section 1†).

### Simulation methods

We ran molecular modeling simulations with CHARMM<sup>25</sup> version 29 software with PARAM19 force field.<sup>25</sup> In all MD simulations the solvation effect was incorporated by using the analytic continuum electrostatics (ACE2)<sup>26,27</sup> module in CHARMM.<sup>28</sup> It calculates the solvation free energy including the entropic contribution from water, based on a linearized treatment of the generalized Born solvation model, which has been shown to describe solvation effect properly unless there are specific effects mediated by discrete water bridges.<sup>29,30,31,32</sup> Histidine residues were protonated, to account for the experimental condition of neutral pH. The filament structures were constructed as a  $\beta$ -sheet bilayer using 15 peptides on each sheet. As described previously, backbone hydrogen bonds between peptides on each sheet were formed between the RAD16-I part of the peptide,<sup>14</sup> thus leaving the functional groups to “stick out” from the filament. After building the filament structure, the system was initially energy-minimized for 200 steps using the steepest descent method, followed by 3000 steps of the adopted-basis Newton-Raphson (ABNR) method. The system was then heated from 0 K to 300 K over 100 ps, and equilibrated for 300 ps. The final production run lasted for 1 ns with the leap-frog integration method using a time step of 2 fs, and a frequency of saving coordinates of 0.8 ns. Simulations were repeated five times

for each peptide with different values of random number seeds. Moreover 200 ps MD simulations for each peptide were run at different temperatures (300 K, 350 K, 400 K and 450 K), to test the stability of the structure (data not shown). Lengths of the bonds connecting hydrogens to heavy atoms were fixed by using the SHAKE algorithm.<sup>33</sup> Visualization of molecular conformations, each one representative of the five runs, and MD trajectories were performed using VMD.<sup>34</sup> A long equilibration period of the aligned peptides in extended conformations was to ensure full relaxation of the initial structure. A separate, 2 ns MD at 450 K was performed on a single peptide and the solvent accessible surface area (ASA) of the side-chains was calculated every 80 ps. To calculate ASA, we used the algorithm of Shrake and Ripley,<sup>35</sup> with a probe of radius 1.4 Å. We also calculated the mean ASA per residue as a function of time as another indicator of the average solvent accessible surface area of each peptide.

### Atomic force microscopy

FPs at a concentration of 1% w/v solution were diluted (at a ratio of 1:100) in sterile water and 5  $\mu$ l of these solutions were placed on mica muscovite substrates and kept at room temperature for 1 minute. The mica surfaces were then rinsed with Millipore-filtered water to remove loosely bound protein and dried under a stream of gaseous nitrogen.

Mica is widely used in atomic force microscopy (AFM) with biological samples because it absorbs proteins on its surface with sufficient strength to retain the protein.

AFM images were collected in tapping<sup>TM</sup> mode by a Multi-Mode Nanoscope IIIa (Digital Instruments) under a dry nitrogen atmosphere using single-beam silicon cantilever probes (Veeco RTESP: resonance frequency 300 KHz, nominal tip radius of curvature 10 nm, force constant 40 N/m). If necessary, data sets were subjected to a first-order flattening.

Measured fiber dimensions were corrected because of the convolution effect arising from the finite size of the AFM tip. The observed nanofiber heights being far lower than the tip radius (10 nm), the observed widths can be corrected with the formula:<sup>36</sup>

$$\Delta x = \sqrt{2[h(2r_t - h)]} \quad (1)$$

where  $\Delta x$  is the width broadening effect,  $h$  is the nanofiber height, and  $r_t$  is the tip radius.

The diameter of globular aggregates has to be corrected with the formula:<sup>36</sup>

$$R = w^2/(16r_t) \quad (2)$$

where  $R$  is the corrected radius,  $w$  is the measured width, and  $r_t$  is the tip radius. In both cases the tip is assumed to be a perfect sphere and fibers are considered as tabular structures, and aggregates as spherical ones.

### Raman measurements

Raman spectra were collected both on solutions and on dried samples obtained either from water evaporation or 12 h treatment in a lyophilizer (Labconco). Powder samples were deposited on a silicon wafer after the latter procedure gave the best

signal-to-noise ratio with no interference from the water phonon spectrum. No detectable modification of the Raman pattern resulted from water removal. Measurements were carried out using the 632.8 nm line of a He-Ne laser as the light source and collecting the scattered light signal in backscattering geometry by a Raman spectrometer (Labram Dilor). The laser was focused on the sample with a spot diameter of about 2  $\mu\text{m}$ . Care was taken to avoid laser induced sample heating. For this purpose, direct measurements of the sample temperature in the chosen experimental configuration at various laser power values and exposure times were collected analyzing the ratio between Stokes and anti-Stokes Raman modes of reference samples. In all cases the estimated sample temperature was lower than 30  $^{\circ}\text{C}$ . The signal was detected by means of a CCD (Jobin-Yvon Spectrum One 3000), with a spectral resolution of 1  $\text{cm}^{-1}$ , by averaging 10 spectra obtained with an acquisition time of 180 s each. Background from the silicon micro-Raman spectrum, although almost negligible in the investigated 900–1800  $\text{cm}^{-1}$  spectral range containing the main features of the protein spectra, was subtracted. Spectra were then normalized to the peak at  $\sim 970 \text{ cm}^{-1}$  from C–C stretching.

A protein's vibration mode, amide I band, appears in the 1600–1700  $\text{cm}^{-1}$  region of the Raman spectrum. This region is a function of the secondary structure of the protein. The amide I region was fitted with Origin 7. A Gaussian interpolation function was employed.

The amide I band at  $\sim 1610 \text{ cm}^{-1}$ , accounting for ring modes from Phe and Tyr side-chains, has been included along with other amide I bands only when necessary (for RADA16-I-BMHP1 and RADA16-I-ALK). The region considered in the band fitting procedure goes from 1630  $\text{cm}^{-1}$  to 1700  $\text{cm}^{-1}$ . The baseline from 1550  $\text{cm}^{-1}$  to 1750  $\text{cm}^{-1}$  was assumed to be linear. Comparison of the  $\chi^2$  values and  $R^2$  value was used as the criteria for assessing the quality of fit.

## Results and discussion

Four different self-assembling peptides, comprising a self-assembling sequence and three functionalized versions of the same self-assembling “core”, showing various hydrophobic profiles at their added functional motifs, have been analyzed (Fig. 1A) *via* molecular dynamics in order to understand the stability of their self-assembled nanofibers. We then investigated their self-assembled molecular structure *via* Raman spectroscopy and atomic force microscopy, which gave results consistent with MD simulations, showing a strong influence of the functional motif over the self-assembling capacity of the same self-assembling core.

In details, hydrophobicity profiles of the FPs show the different hydrophobicity distribution of each added functional motifs. RADA16-I-SDE peptides show charged or neutral residues, while RADA16-I-BMHP1 and RADA16-I-ALK have balanced functional motifs, and, notably, RADA16-I-ALK peptides show the most hydrophobic residues of the all four (Fig. 1B). While all of the FPs were soluble (at 1% w/v concentration), only RADA16-I and RADA16-I-BMHP1 formed macroscopic hydrogels when phosphate buffer saline solution (PBS, pH 7.4) was added to the FP solutions.

While previous studies confirm our macroscopic findings for RADA16-I and RADA16-I-BMHP1<sup>10,21</sup> more detailed tests should provide insights into the assembly of the other FPs, if any, involving a limited number of molecules and consequently not necessarily giving rise to any macroscopic scaffold.

## Molecular dynamic simulations

We constructed filaments using the cross- $\beta$  structure proposed by Park and colleagues, with the RADA16-I part arranged to form a  $\beta$ -sheet bilayer (see ESI section 2†). While these filaments can form larger bundles in experiments, differences in their self-assembling propensity manifest at the single-filament level.<sup>11,14</sup> Thus our simulation on the behavior of pre-formed filaments should give an indicator of the stability of self-assembled fibers of the constituent peptides. During MD, the three filaments exhibited different conformational behaviors (Fig. 2). Although not all FPs assembled into filaments in experiments, imposing a filament structure and monitoring its stability in simulations is a way to infer how each functional group affects their stability. For RADA16-I-BMHP1 and RADA16-I-ALK, the  $\beta$ -sheet bilayer structure of the RADA16-I part remained stable during the simulation period (Fig. 2A and B), this was observed for temperatures up to 450 K.

The balance between hydrophobic and hydrophilic interactions plays a pivotal role in controlling the aggregation propensity and the aggregate morphology: if the added group is too hydrophobic, while aggregation is promoted, it is difficult to form an ordered fibril, since it is kinetically easier to form globular aggregates. On the other hand, strongly hydrophilic groups prevent aggregation and may impair the solubility of the peptides. To better understand the influence of the peptide sequence on self-assembly, we monitored the ASA of a single peptide molecule over 2 ns MD simulations at 450 K (calculated every 80 ps; Fig. 3). The overall ASA profiles were consistent with the hydrophobicity of the peptides. In the case of the most hydrophobic RADA16-I-ALK, the profile changed the least over the course of the simulation, maintaining one broad region of low ASA (AA 14–19), suggesting that the peptide underwent hydrophobic collapse right after the simulation started (blue bands Fig. 3B). The less hydrophobic RADA16-I-BMHP1 shows overall a higher ASA (average 55  $\text{\AA}^2$ ) (Fig. 3A), although it is smaller than the most hydrophilic RADA16-I-SDE (average 97.74  $\text{\AA}^2$ ). When the ASA per residue as a function of time was considered (ESI section 3†), at 160 ps, RADA16-I-SDE had 106  $\text{\AA}^2$  while RADA16-I-BMHP1 and RADA16-I-ALK respectively had 87  $\text{\AA}^2$  and 75  $\text{\AA}^2$ . Moreover at 1000 ps, RADA16-I-SDE maintained a large ASA (100  $\text{\AA}^2$ ) till the end of simulation. RADA16-I-ALK also maintained an ASA of 58  $\text{\AA}^2$  per residue till the end. RADA16-I-BMHP1 remained stable, around a value of 76  $\text{\AA}^2$  and only near 1600 ps did its ASA per residue drop to 60  $\text{\AA}^2$ .

The swift hydrophobic collapse of the RADA16-I-ALK molecule suggests that this peptide likely forms disordered aggregates since it would be difficult to self-assemble into double layer  $\beta$ -sheet structured nanofibers after the competing formation of random clusters. On the other hand, as individual RADA16-I-BMHP1 molecules explore wider conformational space, upon aggregation, they can still rearrange and make

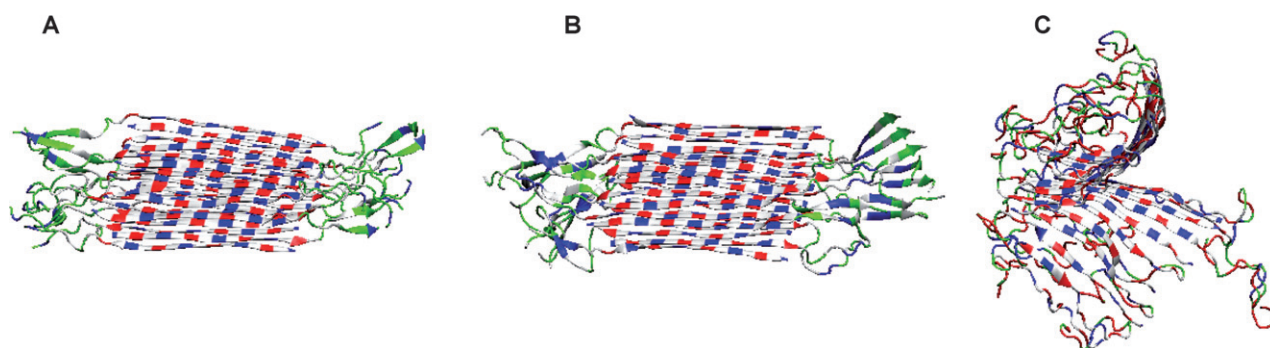


**Fig. 2** Final conformations of initially imposed  $\beta$ -sheet bilayer structures (15 molecules on each side) after 1 ns MD simulations. (A) RADA16-I-BMHP1, (B) RADA16-I-ALK, (C) RADA16-I-SDE. Color schemes for residues are: blue (basic), white (hydrophobic), red (acidic), and green (polar). In the “cartoon” representation arrows represent  $\beta$ -sheet structures. Notably, in (A) and (B) the functional groups form clusters and the bilayer structure remained stable during MD, while in (C) no clusters were formed among the functional groups and the two layers split.

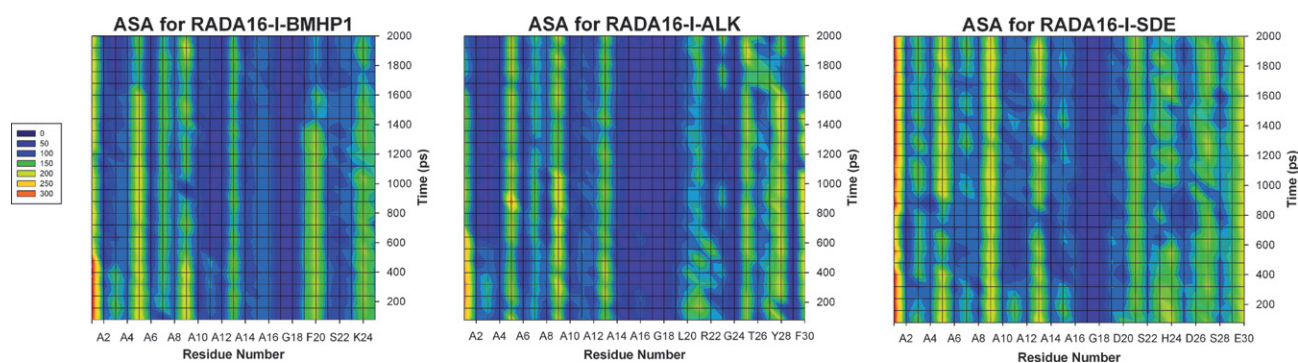


**Fig. 3** ASA profiles of individual side-chains (single molecules for each investigated peptide) over 2 ns MD at 450 K. ASA calculations were obtained every 80 ps.

a transition into ordered fibrils. Our analysis of the ASA profile corroborates the proposed role of the balance between hydrophobic and hydrophilic interactions. Also, the effect of conformational flexibility of individual molecules—from RADA16-I-ALK (collapsed), to RADA16-I-SDE (random coil like)—is consistent with the view that partial denaturation of protein is an important condition for amyloid fibril formation.<sup>6,22</sup>

### AFM analysis

AFM imaging showed remarkably different nanostructures among the four tested self-assembling peptides (Fig. 4). RADA16-I, the self-assembling “core” shared by the other FPs, forms nanofibers (Fig. 4A), as widely described in previous works.<sup>13</sup> The nanostructure of RADA16-I-BMHP1 (Fig. 4B) looks similar to the RADA16-I structure,<sup>13</sup> in spite of an average nanofiber width ( $14.0 \pm 1.6$  nm) significantly larger than the one measured for RADA16-I nanofibers ( $9.4 \pm 1.2$  nm) whereas fiber thickness is observed to be a multiple of 0.5 nm for both materials. The increase in the nanofiber width is expected as the effect of the added functionalized tails flagging from the self-assembled cores.<sup>21,22</sup> These findings suit the molecular model of self-assembled molecular structures proposed by Zhang and colleagues for RADA16-I and its derived FPs. Width values are expressed as an average of multiple measurements corrected as described in the methods section. It is worth noting that the

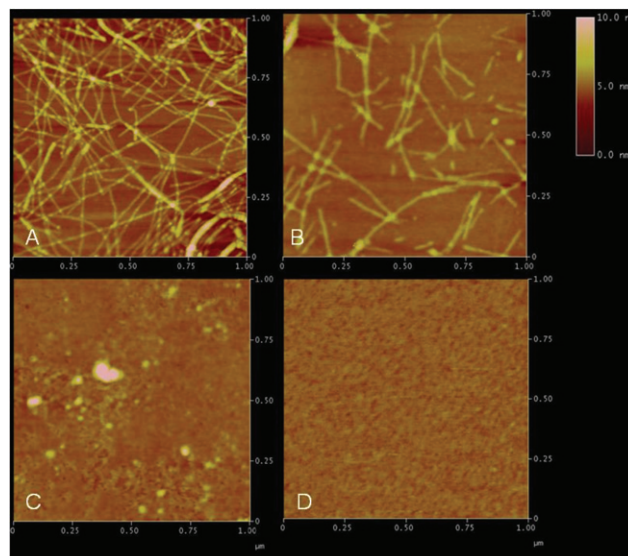


**Fig. 4** AFM images of the tested peptides at a solution concentration of 1% (w/v). (A) RADA16-I self-assembles into nanofibers (average width:  $\sim 10$  nm). (B) RADA16-I-BMHP1 self-organizes into nanofibers larger than those shown in (A) ( $\sim 15$  nm wide), this increase is due to the addition of the functional motif at the C-terminal. (C) RADA16-I-ALK aggregates into globular structures of  $\sim 15$  nm average diameter. (D) RADA16-I-SDE evenly coats the mica surface.

observed fibrillar assemblies give rise to fibers with multiple heights due to the formation of multiple layers, while the pace of these same heights is consistent with a double  $\beta$ -sheet model.

On the other hand the RADA16-I-ALK nanostructure shown in Fig. 4C is remarkably different from those previously described. Indeed, RADA16-I-ALK molecules make globular aggregates rather than nanofibers and, as no recurrent lengths of these round-shaped aggregates have been detected, they seem to be non-ordered structures. In order to provide an indication of the average size of these aggregates, we considered their shape as actually spherical. The observed globes showed a widely spread size distribution; however, the average size of the aggregated particles is  $15 \pm 2$  nm. It is noteworthy that even isolated tiny particles were observed.

The globular shape of RADA16-I-ALK can be explained by the increased hydrophobicity given by the added functional motif. Compared to other inter-molecular forces such as electrostatic and van der Waals interactions, hydrophobic interactions are longer-ranged<sup>4,37</sup> thus is more relevant to earlier steps of aggregation. Indeed, as shown by the MD and the achieved stable ASA conformation, it is possible that the strong hydrophobic effect in RADA16-I-ALK promotes aggregation toward a kinetically trapped, globular structure rather than into more ordered fibrils,<sup>26</sup> thus exposing a decreased surface area to the solvent. To kinetically favor the formation of fibers for RADA16-I-ALK additional AFM experiments were performed at peptide concentrations of 1% w/v. Indeed sporadic nanofibers were detected at such a high concentration (ESI, section 4†). Still nanofiber formation for RADA16-I-ALK can be considered as a secondary phenomenon if compared to the occurrence of nanostructures in the case of RADA16-I and RADA16-I-BMHP1. RADA16-I-ALK fiber thickness is similar to RADA16-I and the average fiber width ( $19 \pm 1.5$  nm) is consistent with a cross- $\beta$  molecular structure. This experimental finding is in accordance with the MD data, where a statistically favored self-assembled nanofiber is a stable secondary structure.

RADA16-I-SDE (Fig. 4D) exposure to PBS did not induce a detectable assembled nanostructure; however, an accurate observation of the sample surface and a comparison with images acquired under the same conditions on the bare mica surface evinced that a uniform layer (rms: 0.2 nm) formed on the mica surface. In order to confirm the presence of the peptide over the mica surface we managed to dig a square on the sample surface and measure the thickness of the layer itself (ESI section 5†). These measurements confirmed that RADA16-I-SDE formed a uniform monolayer on the mica surface. RADA16-I-SDE did not arrange itself in a definite structure as indicated by the MD. The scarce self-assembling propensity of this FP is rather expected: ASA calculations show a high and varying surface area exposed to the solvent. The highly hydrophilic SDE motif added to RADA16-I perturbs the otherwise stable structure of RADA16-I.

### Raman spectroscopy

We investigated the molecular vibrational modes evinced in the Raman spectra of the investigated materials in the range 900–1800  $\text{cm}^{-1}$  (Fig. 5). Several peaks and structured bands fell in this spectral region forming the patterns typically observed in

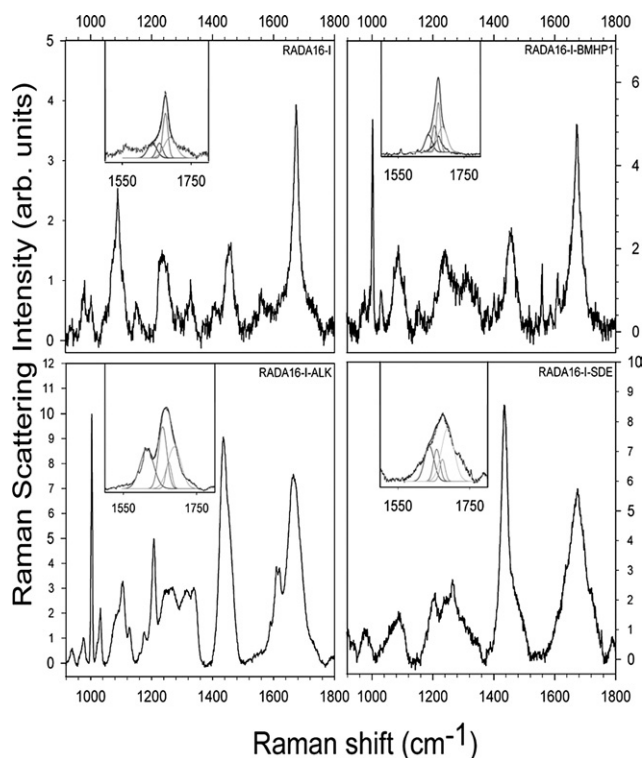


**Fig. 5** Raman spectra (900–1800  $\text{cm}^{-1}$  region) of the tested self-assembling peptides. Insets: deconvolution of the Amide I region (1500–1800  $\text{cm}^{-1}$ ) for each spectra. Each spectra shows the typical features of proteins: Amide I and Amide III peaks are clearly visible (respectively  $\sim 1600$ – $1700$   $\text{cm}^{-1}$  and  $1200$ – $1300$   $\text{cm}^{-1}$ ). (A) RADA16-I and (B) RADA16-I-BMHP1 show similar spectra with the exclusion of the aromatic features given by the Phe residue in the amino acid sequence of RADA16-I-BMHP1. (C) RADA16-I-ALK and (D) RADA16-I-SDE spectra are significantly different from (A) and (B) especially in the region of  $\text{CH}_2$  and  $\text{CH}_3$  bending vibrational mode. Indeed peak intensity in this region appears to be correlated to the self-assembly propensity of FPs, showing higher values in FPs that do not self-assemble.

proteins (Table 1), with spectral features grouped in contributions given by vibration modes of the backbone structures from C–C and C–N stretching<sup>38</sup> in the range 900–1100  $\text{cm}^{-1}$ , combination modes from C–N stretching and N–H bending involved in the peptide backbone in the range 1200–1300  $\text{cm}^{-1}$  (amide III region),<sup>39</sup> bending modes associated with  $\text{CH}_2$  and  $\text{CH}_3$  deformation in the 1300–1500  $\text{cm}^{-1}$  regions, and C=O stretching mode at 1600–1700  $\text{cm}^{-1}$  in the amide I region.<sup>31</sup> Further peaks were observed in two FPs (RADA16-I-BMHP1 and RADA16-I-ALK) due to ring vibrations of aromatic side-chains.<sup>40</sup> Information on the secondary structure of peptides can be obtained from the analysis of the amide regions.<sup>41</sup> Particularly, the shape of the amide I band gives evidence of the contributions from  $\alpha$ -helices,  $\beta$ -sheets, and unstructured  $\beta$ -strands.<sup>42</sup> Indeed, peak conformation and possible asymmetry of the amide I band suggest a distribution of secondary structures. The analysis in Gaussian components showed that this region is satisfactorily reproduced by three main components with spectral positions and bandwidths reported in Table 2, besides added components accounting for aromatic residues. The results of the analysis are consistent with findings from previous works demonstrating that

**Table 1** Raman spectra peaks interpretation for the observed dehydrated peptides

RADA16-I Raman shift (cm <sup>-1</sup> )	RADA16-I-BMHP1	RADA16-I-ALK	RADA16-I-SDE	Assignments <sup>a</sup>
1674	1673	1664	1675	Amide I
	1610	1609		Phe/Tyr
1460	1457	1453	1434	δCH <sub>2</sub>
1405	1405	1404	1405	νCOO <sup>-</sup>
1327	1315	1314	1313	νCH <sub>2</sub>
1237	1240	1269	1264	Amide III
	1205	1207		Phe/Tyr
	1157	1173		Phe/Tyr
1088	1086	1105	1086	νC-C/νC-N
	1028	1031		Phe
	1001	1003		Phe
980	975	975	974	νC-C
939	939	938	922	νCα-C-N

<sup>a</sup> Peak assignment are based on previous papers.<sup>34</sup> Abbreviations: ν = stretching mode, δ = deformation, γ = in plane bending. Phe = phenylalanine, Tyr = tyrosine.

**Table 2** Band fitting and comparison of Amide I region of different FPs<sup>a</sup>

FP	Center (cm <sup>-1</sup> )	Width (cm <sup>-1</sup> )	% Area
RADA16-I	1658	18	18.86
	1675	15	40.34
	1689	35	40.80
RADA16-I-BMHP1	1658	18	25.20
	1675	15	12.30
	1689	35	37.55
RADA16-I-ALK	1658	22	42.20
	1674	15	12.30
	1689	35	45.50
RADA16-I-SDE	1658	18	20.10
	1674	15	11.90
	1689	35	68.00

<sup>a</sup> Amide I region was fitted considering the three symmetrical components representing three different structural conformations of proteins: α-helix (1658 cm<sup>-1</sup>), β-sheet (1675 cm<sup>-1</sup>) and extended β-strand and PPII structure (1689 cm<sup>-1</sup>).

the band at 1658 cm<sup>-1</sup> is a marker of α-helices, the band around 1670 cm<sup>-1</sup> is associated to β-sheets, while the broad band at higher energy is due to unstructured β-strands. A component above 1700 cm<sup>-1</sup> arises from C=O stretching from aspartic and glutamic acids and is observed as a shoulder of the amide I band in the spectra of Fig. 5. Ionization of carboxylic groups in side-chains may shift this mode to a lower energy frequency at about 1405 cm<sup>-1</sup>.<sup>42</sup> However no relevant contribution of this component was observed.

The different relative intensities of the components in the amide I band reveal a different propensity of the four peptides to take α-helix, β-sheet and unstructured β-strand as their secondary conformation. Specifically, RADA16-I-BMHP1 shows a band shape quite similar to the parent molecule, RADA16-I. The band is dominated by the narrow peak at 1674 cm<sup>-1</sup>, ascribable to C=O stretching in β-sheet aggregation, consistent with the formation of fibers observed in AFM images. The peak broadening in the amide I region is instead peculiar to the spectra of RADA16-I-ALK and RADA16-I-SDE and evinces the predominance of conformations dissimilar to β-sheet ones. By comparing Raman spectra and AFM images, this

broadening appears as a clear-cut marker of the failure of fiber self-assembling. Band deconvolution (Table 2) gives further insights on the behavior of these functionalized peptides. In fact, the band broadening is different for the two FPs, and the intensity ratio between the components at 1655 and 1690 cm<sup>-1</sup> drastically changes, indicating that the unstructured β-strand conformation is dominant in RADA16-I-SDE, while molecule torsions typical of the α-helix structure are favored in RADA16-I-ALK functionalized peptides. As AFM does not provide any reliable clue concerning the secondary structures of these molecules Raman analysis completes the information necessary to understand their assembling propensity. The Raman analysis suggests that the lack of aggregates in the AFM image of RADA16-I-SDE material has to be related to the high hydrophilic features of this FP, since the largely preferred unstructured β-strand random conformation reveals that molecules are not forced by the solvent to adopt a specific shape and consequently to arrange themselves in a secondary structure. A drastically different situation occurs in RADA16-I-ALK material, since AFM images showed aggregates, and sporadic nanofiber formation was detected at higher peptide concentrations. The relatively large contribution of the α-helix component in the amide I band, coexistent with the main contribution from unstructured β-strand random conformation, strongly suggests that the molecule backbones do not take part in an ordered assembled structure. Therefore, the observed aggregates probably do not result from ordered self-assembling interactions among molecules, but rather from the nucleation of disordered aggregates formed by molecules whose internal conformation is mainly driven by the single molecule hydrophobic tails exposure to the solvent, with no relevant inter-molecular interactions.<sup>44</sup>

In this regard, Raman spectrum analysis in the spectral region of CH<sub>2</sub> and CH<sub>3</sub> deformation modes may give new tools to understand the behavior of this class of FPs. Even though this spectral region has not been considered in the past in the investigation of peptide conformations, it is apparent from Fig. 5 that the relative intensity of the deformation band peaked at approximately 1440 cm<sup>-1</sup> is strongly dependent on the peptide sequence. Specifically, this band is more intense, by a factor 3–4, in materials with no fiber self-assembling (RADA16-I-ALK and

RADA16-I-SDE), with also a drastic change of relative intensity if compared with other peptide structures in the phonon spectrum. Indeed this appears as the main feature of non self-assembling peptides. These differences cannot be imputed to the different number of CH<sub>2</sub> and CH<sub>3</sub> groups in the different molecules. Indeed, the CH<sub>2</sub>/CH<sub>3</sub> calculated number, normalized to the peptide length, gives no notably different values within the set of investigated molecules, showing the maximum positive variation of 20% for RADA16-I, contrary to the relative intensities observed. Similar intensity changes of methyl deformation modes were reported by Pézolet and colleagues concerning poly-L-lysine in solutions at different pH values.<sup>43</sup> Although the work of McGarvey's group was focused on other spectral features, the reported results strongly support that the 1440 cm<sup>-1</sup> intensity change is strictly related to the pH-induced conformation change of poly-lysine. In order to verify the relevance of those results in our investigation, we reproduced the same measurements of poly-L-lysine in the experimental configuration we used to investigate our FPs and results confirmed the effect. Specifically, we observed that CH<sub>2</sub> and CH<sub>3</sub> deformation modes appear extremely sensitive to self-assembling, showing higher intensity in non-assembled structures, either  $\alpha$ -helix or  $\beta$ -strand, than in  $\beta$ -sheet fibers. This is related to a larger Raman cross section of CH<sub>2</sub> bending modes in free configuration compared with situations where molecules are faced and linked along the backbone through hydrogen bonds. Following this approach, the high intensity in RADA16-I-ALK material gives an important insight on the origin of the inhomogeneous aggregation observed in AFM images, suggesting that the aggregates are formed by randomly interacting molecules. The molecules are forced in to  $\alpha$ -helix and disordered  $\beta$ -strand conformations by their hydrophobic nature, and are kept together mainly by hydrophobic forces, without relevant reciprocal interactions. Raman data give evidence that strong hydrophobic features of RADA16-I-ALK induce the formation of intra-molecular conformations that prevent the peptide self-assembling in  $\beta$ -sheets, even though  $\beta$ -sheet inter-molecular interactions may probably be stable once they are formed, as suggested by the results of MD and AFM as is clear from the ESI section 3.†

## Conclusions

Results of molecular dynamics simulations gave precious indications regarding the stability of assembled nanofibers of three FPs, which are strongly affected by their hydrophobicity profiles. They also provided insights into the AFM and Raman results. In both MD and AFM imaging, RADA16-I-BMHP1 maintained the  $\beta$ -sheet bilayer filament structure typical of its self-assembling "core" RADA16-I. In contrast, simulation of the RADA16-I-SDE filament showed a marked propensity to open the initial bilayer conformation, likely caused by solvation forces on the hydrophilic groups. In the AFM images, RADA16-I-SDE did not form organized nanostructures; it rather appeared to evenly cover the mica surface. At the end of the MD, RADA16-I-ALK showed a final molecular configuration similar to that of RADA16-I, but the AFM analysis revealed different globular structures of heterogeneous sizes. Differences in hydrophobicity were also assessed by ASA calculations, whose time dependence is related to the kinetics of folding. Slow folding appears to be

essential for constructing organized multi-molecular structures, as fast hydrophobic collapse resulted in globular aggregates. Other studies will be necessary in the future to understand if there is a way to increase the formation of nanofibers formed by RADA16-I-ALK. Raman spectroscopy measurements were performed to analyze with more details the secondary structure of the tested FPs. The decreased  $\beta$ -sheet structure component, showed *via* the deconvolution of the Amide I region for RADA16-I-ALK and RADA16-SDE peptides, suggested a minor tendency to form  $\beta$ -sheet double layers: indeed intra-molecular interactions (mainly  $\alpha$ -helix conformations) appeared to be preferred. Moreover, taking into account the CH<sub>2</sub> deformation region, a CH<sub>2</sub>/CH<sub>3</sub> bending vibrational mode of RADA16-I-ALK and RADA16-SDE spectra, significantly different from its counterpart in RADA16-I and RADA16-I-BMHP1 spectra, suggests a critical role played by this mode in the self-assembling process. MDs provided indications of the stability of assembled cross- $\beta$  structures of the chosen peptides and Raman micro-spectroscopy gave precious insights about the secondary structure of apparently similar self-assembling peptides. Raman spectroscopy data, in accordance with AFM findings and MD simulations, provided new intriguing possibilities for investigating in aqueous solutions or the lyophilized state the self-assembled structures of FPs, new promising biomaterials for tissue engineering, drug delivery and other applications. FP design requires a better understanding of their secondary structure formation as a consequence of the added functional motifs. By synergistic use of these three different investigation techniques strategies for designing and synthesizing novel functionalized self-assembling biomaterials were proposed and innovative new ones can be developed.

## Acknowledgements

The overall project is supported by the CARIPLO foundation and conducted at the facilities of University of Milan – Bicocca and TAMU University.

## References

- 1 R. P. Langer, R. Lanza and J. P. Vacanti, *Principles of Tissue Engineering*, Academic Press Inc, San Diego, CA (USA), 2nd edn, 2000.
- 2 X. Zhao and S. Zhang, *Trends in Biotechnol.*, 2004, **22**, 470–476.
- 3 F. Gelain, A. Hori and S. Zhang, *Macromolecular Bioscience*, 2007, **7**, 544–551.
- 4 J. N. Israelachvili, *Intermolecular and Surface Forces: With Applications to Colloidal and Biological Systems*, Academic Press, Inc, London (UK), 2nd revised edn, 1985.
- 5 S. Zhang, T. Holmes, C. Lockshin and A. Rich, *Proc. Natl. Acad. Sci. USA*, 1993, **90**, 3334–3338.
- 6 R. Fairman and K. Askerfeldt, *Curr. Opin. Struct. Biol.*, 2005, **15**, 453–463.
- 7 B. Law, R. Weissleder and C. H. Tung, *Biomacromolecules*, 2006, **7**(4), 1261–1265.
- 8 J. D. Hartgerink, E. Beniash and S. I. Stupp, *Science*, 2001, **294**, 1684–1688.
- 9 S. Pujals, J. Fernández-Carneado, M. D. Ludevid and E. Giralt, *Chem. Med. Chem.*, 2008, **3**(2), 296–301.
- 10 S. Zhang, T. C. Holmes, C. M. DiPersio, R. O. Hynes, X. Su and A. Rich, *Biomaterials*, 1995, **16**, 1385–1393.
- 11 D. Marini, W. Hwang, D. A. Lauffenburger, S. Zhang and R. D. Kamm, *NanoLetters*, 2002, **2**, 295–299.

- 
- 12 A. Aggeli, I. A. Nyrkova, M. Bell, R. Harding, L. Carrick, T. C. McLeish, A. N. Semenov and N. Boden, *Proc. Natl. Acad. Sci. USA*, 2001, **98**, 11857–11862.
  - 13 H. Yokoi, T. Kinoshita and S. Zhang, *Proc. Natl. Acad. Sci. USA*, 2005, **102**, 8414–8419.
  - 14 J. Park, B. Khang, R. D. Kamm and W. Hwang, *Biophys. J.*, 2006, **90**, 2510–2524.
  - 15 O. S. Makin and L. C. Serpell, *FEBS J.*, 2005, **272**, 5950–5961.
  - 16 P. A. Temussi, L. Masino and A. Pastore, *EMBO J.*, 2003, **22**(3), 355–361.
  - 17 A. L. Sieminski, C. E. Semino, H. Gong and R. D. Kamm, *J. Biomed. Mater. Res.*, 2008, **87A**, 494–504.
  - 18 C. E. Semino, J. Kasahara, Y. Hayashi and S. Tissue Eng., 2004, **10**, 643–655.
  - 19 M. E. Davis, J. P. Motion, D. A. Narmoneva, T. Takahashi, D. Hakuno, R. D. Kamm, S. Zhang and R. T. Lee, *Circulation*, 2005, **111**, 442–g2450.
  - 20 T. Kreis and R. Vale, *Guide book to the extracellular matrix, anchor, and adhesion proteins*, Oxford University Press, Oxford, UK, 2nd edn, 1999.
  - 21 F. Gelain, D. Bottai, A. L. Vescovi and S. Zhang, *PLoS ONE*, 2006, **1**, e119.
  - 22 A. Horii, X. Wang, F. Gelain and S. Zhang, *PLoS ONE*, 2007, **2**(2), e190.
  - 23 M. Apetri, N. Maiti, M. Zagorski, P. Carey and V. E. Anderson, *J. Mol. Biol.*, 2006, **355**, 63–71.
  - 24 W. C. Wimley and S. H. White, *Nature Struct Biol*, 1996, **3**, 342–848.
  - 25 B. R. Brooks, R. E. Brucoleri, B. D. Olafson, D. J. States, S. Swaminathan and M. Karplus, *J. Comp. Chem.*, 1983, **4**, 187–217.
  - 26 M. Schaefer and M. Karplus, *J. Phys. Chem.*, 1996, **100**, 1578–1599.
  - 27 M. Schaefer, C. Bartels, F. Leclerc and M. Karplus, *J. Comp. Chem.*, 2001, **22**, 1857–1879.
  - 28 W. Hwang, S. Zhang, R. D. Kamm and M. Karplus, *PNAS*, 2004, **101**, 12916–12921.
  - 29 N. Calimet, M. Schaefer and T. Simonson, *Proteins*, 2001, **45**, 144–158.
  - 30 M. Schaefer, C. Bartels, F. Leclerc and M. Karplus, *J. Comput. Chem.*, 2001, **22**, 1857–1879.
  - 31 B. Roux and T. Simonson, *Biophys. Chem.*, 1999, **78**, 1–20.
  - 32 W. Hwang, D. M. Marini, R. D. Kamm and S. Zhang, *J. Chem. Phys.*, 2003, **118**, 389–397.
  - 33 J. P. Ryckaert, G. Ciccotti and H. J. C. Berendsen, *J. Comput. Phys.*, 1977, **23**, 327–341.
  - 34 W. Humphrey, A. Dalke and K. Schulten, *J. Molec. Graphics.*, 1996, **14**, 33–38.
  - 35 A. Shrake and J. A. Rupley, *J. Mol. Biol.*, 1973, **79**, 351–371.
  - 36 S. Jun, Y. Hong, H. Imamura, B. Y. Ha, J. Bechhoefer and P. Chen, *Biophys. J.*, 2004, **87**, 1249–59.
  - 37 E. E. Meyer, K. J. Rosenberg and J. N. Israelachvili, *PNAS*, 2006, **103**, 15739–15746.
  - 38 D. Canet, A. M. Last, P. Tito, M. Sunde, A. Spencer, D. B. Archer, C. Redfield, C. V. Robinson and C. M. Dobson, *Nat. Struct. Bio.*, 2002, **9**, 308–315.
  - 39 A. Torreggiani, M. Tamba, S. Bonora and G. Fini, *Biopolymers*, 2003, **72**(4), 290–298.
  - 40 M. C. Chen and R. C. Lord, *J. Am. Chem. Soc.*, 1974, **96**, 4750–4752.
  - 41 N. Maiti, M. Apetri, M. Zagorski, P. Carey and V. E. Anderson, *J. Am. Chem. Soc.*, 2004, **126**, 2399–2409.
  - 42 G. Burrafato, M. Calabrese, A. Cosentino, A. M. Gueli, S. O. Troja and A. Zuccarello, *J. Raman Spectrosc.*, 2004, **35**, 879–886.
  - 43 D. Carrier and M. Pézolet, *Biophys. J.*, 1984, **46**(4), 497–506.
  - 44 A. O'Grady, D. Dennis, D. Denvir, J. McGarvey and S. Bell, *Anal. Chem.*, 2001, **73**, 2058–2065.

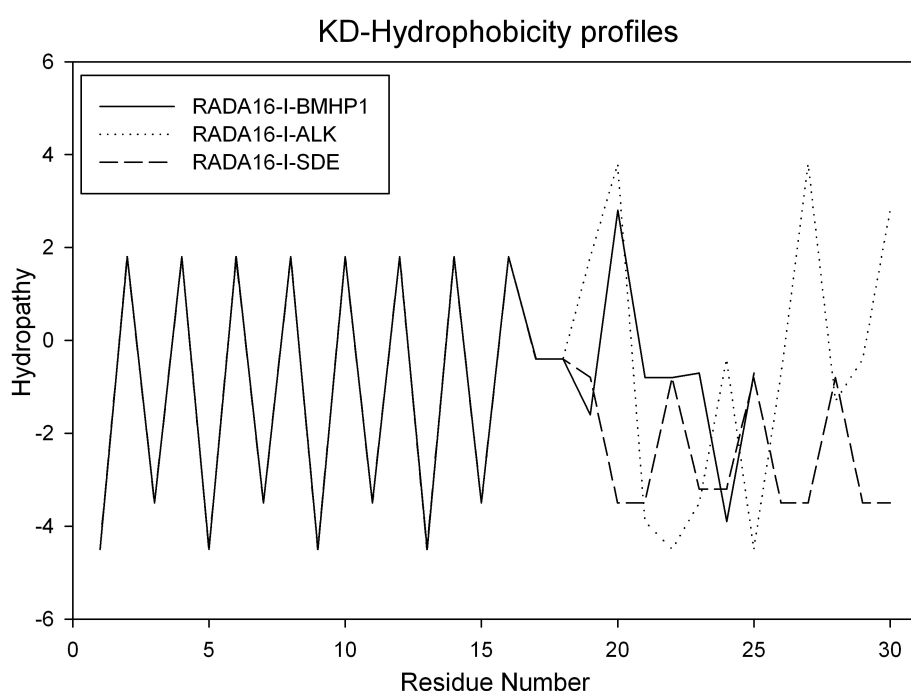
## Supplementary Data

# Effect of functionalization on the self-assembling propensity of $\beta$ -sheet forming peptides

Francesca Taraballi, Marcello Campione, Adele Sassella, Angelo Vescovi, Alberto Paleari, Wonmuk Hwang and Fabrizio Gelain

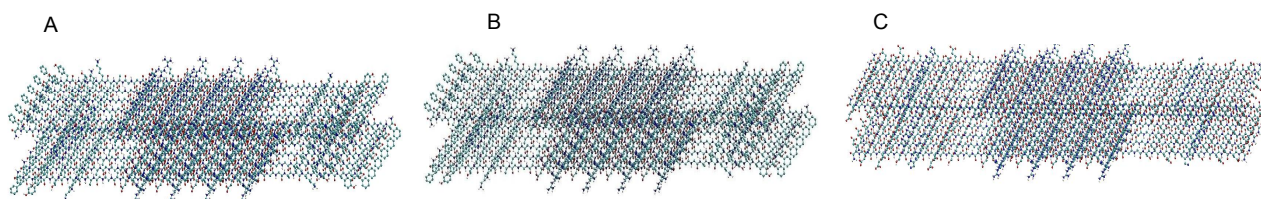
### Section 1

Hydrophobicity profiles calculated via the Kyte-Doolittle scale (J. Kyte and R.F. Doolittle, *J. Mol. Biol.* 1982, **157**,105-132). According to this scale positive values stand for hydrophobic residues while negative values stand for the hydrophilic residues. Hydrophobicity profiles are similar to those obtained with the White and Smith scale.



### Section 2

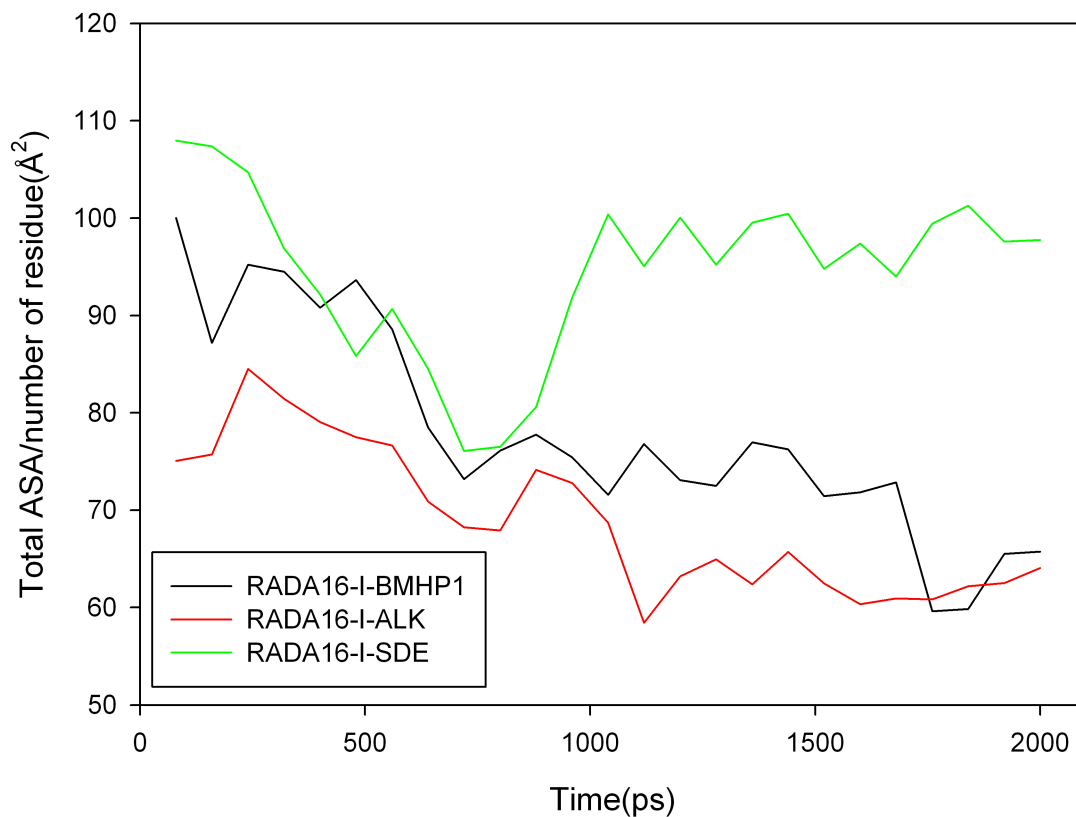
Initial FP arrangement in each MD. The image shows the starting cross- $\beta$  of each peptide in the CPK mode of visualization. A) RADA16-I-BMHP1, B) RADA16-I-ALK, C) RADA16-SDE



### Section 3

Total ASA value normalized over residue number for each peptide. Time step is 80ps.

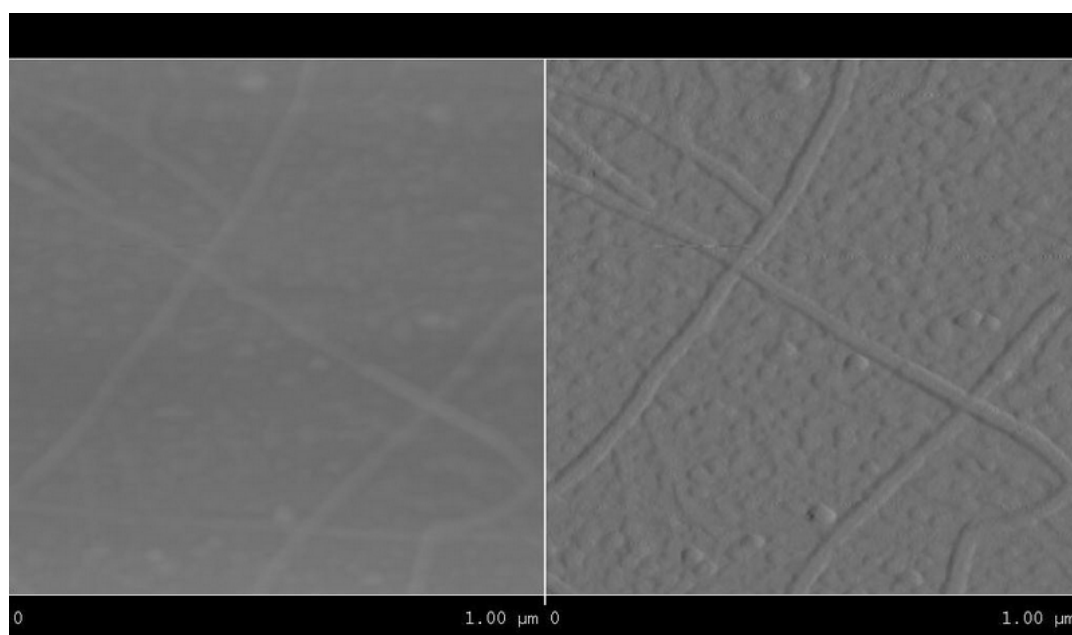
#### Mean ASA for residue calculation



### Section 4

RADA16-I-ALK solution in MilliQ was used to a peptide final concentration of 1% w/v. 5 $\mu$ l peptide solution was placed on mica surface and after 1 minute of adsorption the sample was washed with MilliQ water and dried under a stream of nitrogen.

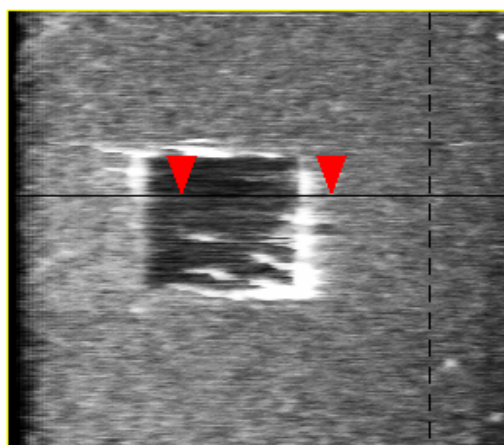
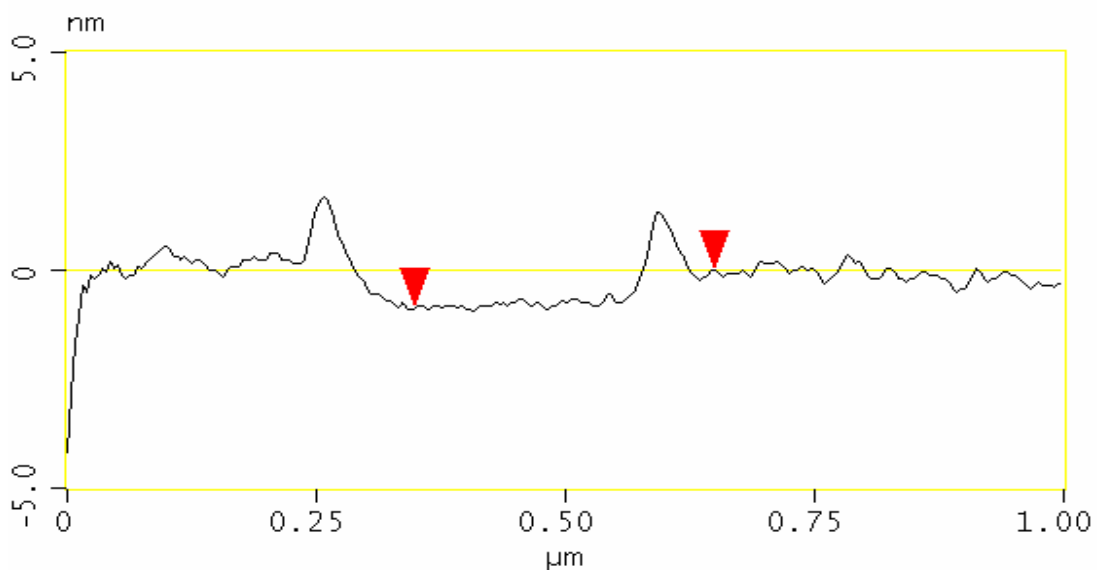
All images were processed using Digital Instrument (Nanoscope 5.31r1) software.



### Section 5

RADA16-I-SDE solution was diluted to a final concentration of 0.01% w/v. 5  $\mu$ l peptide solution was placed on mica surface and after 1 minute of adsorption the sample was washed with MilliQ water and dried carefully under a stream of nitrogen.

All the images were obtained in air in contact mode with a nominal spring constant of 0.16 N/m. All the images were processed using Digital Instrument (Nanoscope 5.31r1) software.



Surface distance	300.94 nm
Horiz distance(L)	300.78 nm
Vert distance	0.880 nm
Angle	0.168 °